scientific reports

OPEN

Solar energy optimization in solar-HVAC using Sutterby hybrid nanofluid with Smoluchowski temperature conditions: a solar thermal application

Wasim Jamshed[1], Mohamed R. Eid[2,3], Rabia Safdar[4], Amjad Ali Pasha[5], Siti Suzilliana Putri Mohamed Isa[6], Mohammad Adil[7,8], Zulfiqar Rehman[9] & Wajaree Weera[10]✉

In solar heating, ventilation, and air conditioning (HVAC), communications are designed to create new 3D mathematical models that address the flow of rotating Sutterby hybrid nanofluids exposed to slippery and expandable seats. The heat transmission investigation included effects such as copper and graphene oxide nanoparticles, as well as thermal radiative fluxing. The activation energy effect was used to investigate mass transfer with fluid concentration. The boundary constraints utilized were Maxwell speed and Smoluchowski temperature slippage. With the utilization of fitting changes, partial differential equations (PDEs) for impetus, energy, and concentricity can be decreased to ordinary differential equations (ODEs). To address dimensionless ODEs, MATLAB's Keller box numerical technique was employed. Graphene oxide Copper/engine oil (GO-Cu/EO) is taken into consideration to address the performance analysis of the current study. Physical attributes, for example, surface drag coefficient, heat rate, and mass exchange are mathematically processed and shown as tables and figures when numerous diverse factors are varied. The temperature field is enhanced by an increase in the volume fraction of copper and graphene oxide nanoparticles, while the mass fraction field is enhanced by an increase in activation energy.

List of symbols

T_∞	Ambient temperature (K)
Re	Reynold's number
Ω	Angular velocity
C_∞	Ambient concentration $\left(\frac{\mathrm{mol}}{\mathrm{m}^3}\right)$
$\dot{\gamma}$	Second invariant strain tensor
e	Consistency index

[1]Department of Mathematics, Capital University of Science and Technology (CUST), Islamabad 44000, Pakistan. [2]Department of Mathematics, Faculty of Science, New Valley University, Al-Kharga, Al-Wadi Al-Gadid 72511, Egypt. [3]Department of Mathematics, Faculty of Science, Northern Border University, Arar 1321, Saudi Arabia. [4]Department of Mathematics, Lahore College Women University, Lahore, Pakistan. [5]Aerospace Engineering Department, King Abdulaziz University, Jeddah 21589, Saudi Arabia. [6]Centre of Foundation Studies for Agricultural Science, Universiti Putra Malaysia, Seri Kembangan, Malaysia. [7]Mechanical Engineering Program, Physical Science and Engineering Division, King Abdullah University of Science and Technology, Thuwal 23955-6900, Saudi Arabia. [8]KAUST Clean Combustion Research Center, King Abdullah University of Science and Technology, Thuwal 23955-6900, Saudi Arabia. [9]Department of Mathematics, Air University, Islamabad 44000, Pakistan. [10]Department of Mathematics, Faculty of Science, Khon Kaen University, Khon Kaen 40002, Thailand. ✉email: wajawe@kku.ac.th

R_δ Thermal radiation
U_w Stretching velocity along x-axis ($\frac{\mathrm{m}}{\mathrm{s}}$)
Pr Prandtl number
σ Reaction rate constant ($\frac{\mathrm{mol}}{\mathrm{lit}\text{-}\mathrm{s}}$)
σ_v Velocity accommodation coefficient
Γ_1 Temperature slip (K)
n Fitted rate constant
T_w Temperature at the wall (K)
μ_0 Zero shear fee viscosity
D_η Deborah number
λ Rotation parameter
E Material time constant
T Temperature
S Extra stress tensor
N Power-law behavior index
Γ_1 Velocity slip ($\frac{\mathrm{m}}{\mathrm{s}}$)
q_r Radiative heat flux ($\frac{\mathrm{W}}{\mathrm{m}^2}$)
E Activation energy ($\frac{\mathrm{J}}{\mathrm{mol}}$)
σ_T Temperature accommodation coefficient
Sc Schmidt number
A_1 Rivilian-Erikson tensor
C_w Concentration at the wall ($\frac{\mathrm{mol}}{\mathrm{m}^3}$)

Researchers have concentrated on new energy measuring to meet the requirements and needs of companies in this period. Researchers are interested in developing a few devices with the highest rate of heating and cooling. These might save and maintain optimal energy efficiency. Furthermore, poor heat transmission and flowing base liquid conducting have an impact on the performance and operation of solar collectors. Many efforts have been made in this respect to improve the thermal characteristics of base liquids. Solar energy is the renewable energy source from the sun for industrial applications such as electricity generation[1–3], heating[4–6], cooling[7–9], and desalination[10–12]. The benefits of solar energy technology are that this type of energy is limitless, clean, and has no fuel to burn. The most common types of solar energy are photovoltaic (PV) systems[13–15], thin-film solar cells[16–18], solar power plants[19,20], and passive solar heating[21,22]. The Photovoltaic applications were reported in the field of telecommunications[23], agriculture[24], used with livestock/cattle[25], street lighting[26], and rural electrification[27]. The usage of thin-film solar cells was in rooftops at the institutional and commercial buildings[28], solar farms[29], power traffics[30], and solar steam generation[31]. Passive solar heating is implemented in circulation spaces such as lobbies, hallways, and break rooms that allow occupants to avoid the sun.

HVAC stands for heating, ventilation, and air conditioning, whereas AC is defined as conditioning. AC is designed to cool the air and control humidity in the house and was invented by Willis Carrier in 1902[32]. Besides, the primary purpose of HVAC system for residential[33,34] and commercial buildings[35,36] is to provide a heating mode in the winter and cooling mode in the summer. This system also filters smoke, odors, dust, airborne bacteria, carbon dioxide, and other harmful gases to improve air indoors[37,38]. In addition, HVAC system acts as a humidity controller of air indoors[39,40]. Meanwhile, the HVAC system powered by solar energy is known as solar-HVAC (S-HVAC), where it is installed by PV panels to capture the sunlight and convert it into electricity. John Hollick is one of S-HVAC innovators, and he patented the method and apparatus for cooling ventilation air for a building[41]. The solar PV panel is connected to the HVAC to convert the solar energy into electricity to power all the parts responsible for the heating or cooling mode in the HVAC. The benefits of the S-HVAC system, instead of traditional HVAC, are lower utility bills, preserve the environment, and ease of installation. HVAC systems have moving parts such as fans and vibrating coils that often break, whereas S-HVAC have fewer moving parts and these systems have fewer breakage risks.

Among the several renewable resources that may be put practically anywhere in the globe, solar power promises to be the major technology for the transition to a decarbonized energy supply. The efficacy of a photovoltaic (PV) system is directly proportional to the amount of solar energy available. Many governments see renewables and energy conservation measures as a viable method to reduce coal consumption. The primary solar devices that can convert sunlight into electricity are PV system and concentrated solar power (CSP). CSP concentrates sun radiation to increase the temperature of a working fluid, and this fluid drives a heat engine and electric generator. CSP generates alternating current (AC), which has a high distribution rate on the power network. Besides, PV collects sunlight through the photoelectric effect to generate electricity in the form of a direct electric current (DC). The DC generated by the PV system is then transformed to AC through the inverters to ensure that the electricity is distributed on the power network. CSP stores energy by using Thermal Energy Storage technologies (TES), and it is not subjected to weather restrictions: This means that CSP can be used at all times (cloudy day, overnight, low sunlight, etc.) to generate electricity. On the other hand, PV system only stores low thermal energy compared to CSP, since it only uses a battery instead of the storage technology like TES. Therefore, CSP has more qualities over PV by performing more noteworthy efficiencies, lower speculation costs, gives warm capacity limit, and a superior mixture activity ability with different energizes to satisfy baseload need around evening time[42].

Parabolic trough solar collector (PTSC) is one type of CSP system that has been used proficiently in water heating[43,44], air-conditioning[45,46], and solar-aircraft[47–51]. PTSC consists of a reflector with a reflecting surface (parabolic-shaped mirror) and a receiver. The reflector collects the incident solar radiation and reflects it onto a receiver located in the focal line of the parabola. The working fluid inside the receiver absorbs the heat from the solar radiation, causing the fluid temperature to increase. Finally, high-pressure superheated steam is generated from this working fluid in a conventional reheat steam turbine-generator to produce electricity. The running fluid in PTSC should have those features: (a) excessive thermal potential and thermal conductivity, (b) low thermal growth and occasional viscosity, (c) strong charge of thermal and chemical properties, (d) minimal charge of corrosive interest and (e) low toxicity[52]. One of the simplest operating fluids in PTSC is innovated nanofluid referred to as hybrid nanofluid and is ready via way of means of submerging specific nanoparticles withinside the equal base fluid. Therefore, there are recent studies regarding the hybrid nanofluid as a working fluid in PTSC installed in solar aircraft[47–51], and when PTSC is equipped with turbulators[53–58]. The following types of hybridizing nanofluid were implemented in the PTSC solar aircraft: Casson hybrid nanofluid[47], Reiner Philippoff hybrid nanofluid[48,49], and tangent hyperbolic hybrid nanofluid[50,51]. Meanwhile, A turbulator is a tool that transforms a laminar boundary layer right into a turbulent boundary layer to optimize heat transfer. Hence, various patterns of turbulators inserted in PTSC were reported, such as single twisted turbulator[53], obstacles act as turbulator[54], finned rod turbulator[55], two twisted tape acts as turbulator[56], inner helical axial fins as turbulator[57], and conical turbulator[58].

When it comes to thermodynamic rules, the second law of thermodynamics is far more dependable than the first law due to its limits of efficiency in heat transmission in industrial applications. This second law is applied to reduce the irreversibility of thermal constructions. Irreversibility is observed in a variety of thermofluidic apparatuses, including thermal solar, air separators, and reactors, and that competence loss is entirely interrelated with it. This generated irreversibility is determined by the rate of entropy production. The extinction of functional energy is measured by entropy generating. Any system's generated irreversibility creates continuous entropy, which eviscerates the functional energy required to execute the job. Such energy loss might be produced by heat transport by convective, conductive, and radiative fluxing. Furthermore, magnetic fields, buoyancy, and fluid friction all contribute to the generation of entropy. As a result, entropy generation minimization is required for diverse thermal equipment to acquire an optimal quantity of energy. The degree of entropy generating in crossbreed nanofluid is impacted by the expansion of twofold nanomaterials into the base liquid. The non-Newtonian cross breed nanofluid heavily influenced by entropy age have been examined, where this type of nanofluid contains the following double nanomaterial and base-fluid: Cu-Al_2O_3/H_2O[59–65], Cu-Al_2O_3/EG[66], Cu-Ag/EG[67,68], Cu-TiO_2/H_2O[69,70], Cu-Ag/H_2O[71], Cu-Go/H_2O[72], Cu-Ti/H_2O, CuO-TiO_2/H_2O and C71500-Ti_6Al_4V/H_2O[73], Cu-Fe_3O_4/EG[74], Cu-CuO/blood[75], Ag-MgO/H_2O[76], Ag-Gr/H_2O[77], CuO-TiO_2/EG[78], Fe_3O_4–Co/kerosene[79], MWCNT-Fe_3O_4/H_2O[80], and MWCNT-MgO/H_2O[81]. The thermal properties of hybrid nanofluid over an elastic curved surface[59], stretching sheet[61,63,70,74,78], disk[64], stretching disk[62], and wedge[79] were reported. In addition, the flow of a hybrid nanofluid in a cavity was investigated under the following conditions: square cavity[68], porous open cavity[69], and vented complex shape cavity[81]. The investigation of a hybrid nanofluid flow through a channel[66] and microchannel[77] have been performed, where these channels are rotating[66], placed vertically[73], and recharging[77]. The flow of a hybrid nanofluid in an enclosure was studied by Alsabery et al.[60], Ghalambaz et al.[65], and Abu-Libdeh et al.[76]. Alsabery et al.[60] implemented the wavy enclosure containing the inner solid blocks, whereas Ghalambaz et al.[65] considered an enclosed cavity with vertical and horizontal parts in their fluid model. On the other hand, Abu-Libdeh et al.[76] selected a porous enclosure with a trapezoid geometry where this type of geometry is used for cooling purposes on the hybrid nanofluid. Meanwhile, Xia et al.[67] and Khan et al.[72] developed the fluid flow model bounded by two rotating parallel frames. The heat analysis of the peristaltic flow of hybrid nanofluid internal a duct become studied through McCash et al.[71]. The electroosmotic pump is involved in the hybrid nanofluid flow studied by Munawar and Saleem[75], with ohmic heating. Shah et al.[80] chose a porous annulus to study the characteristics of a hybrid nanofluid model.

Non-Newtonian fluid models are much more different than those of Newtonianism fluids. The stress values for non-Newtonian fluid are nonlinear functions against strain, yield stress, or time-dependent viscosity. Examples of this type of fluid are Casson fluid[82–86], Maxwell fluid[87–91], nanofluid (also including hybrid case)[47–81], etc. Sutterby fluid model is one type of non-Newtonianism fluid[92], and it describes the viscosity of dilute polymer solutions[93]. Polymer solutions have been applied in related industrial phenomena or products, such as turbulent pipe flows[94,95], stability of polymer jets[96,97], and oil recovery enhancement[98,99]. The heat and mass transfer withinside the flow of magnetohydrodynamics (MHD) Sutterby nanofluid over a stretching cylinder, with the impact of temperature-structured thermal conductivity have been explored by Sohail et al.[100] and Raza et al.[101]. The bioconvection of Sutterby fluid flow was reported when this fluid flows across the wedge[102] and between two rotating disks[103]. Gowda et al.[104], Yahya et al.[105], and Khan et al.[106] incorporated the Cattaneo-Christov heat flux model in their mathematical Sutterby fluid model to archive effective thermal properties. The Cattaneo-Christov heat flux model was developed when the fluid was bounded by a rotating disk[104], flat surface[105], and wedge[106]. The effect of entropy generation and activation energy were considered by Hayat et al.[107]. In contrast, El-Dabe et al.[108] incorporated the boundaries of the attractive field, compound response, permeable media, heat radiation, gooey dissemination, and couple pressure. Parveen et al.[109], Arif et al.[110], Jayadevamurthy et al.[111], Nawaz[112], and Waqas et al.[113] investigated the thermal performance of the Sutterby fluid model with the presence of various hybrid nanoparticles. The base fluid that has become selected was blood[109,110], water[111], and ethylene glycol[112,113]. These researchers[109–113] implemented the dual nanoparticles in their Sutterby hybrid nanofluid, namely as: (i) Au and Al_2O_3[109], (ii) CuO and Al_2O_3[110], (iii) Cu and SiO_2[111], (iv) MoS_2 and SiO_2[112], and (v) first fluid contained SiO_2 and SWCNT, and second fluid used MoS_2 and MWCNT[113].

Motivation

The goal of this study is to look at a Sutterby hybrid fluid traveling along a stretchy surface with copper and graphene oxide nanoparticles. The following are the main points of the current study:

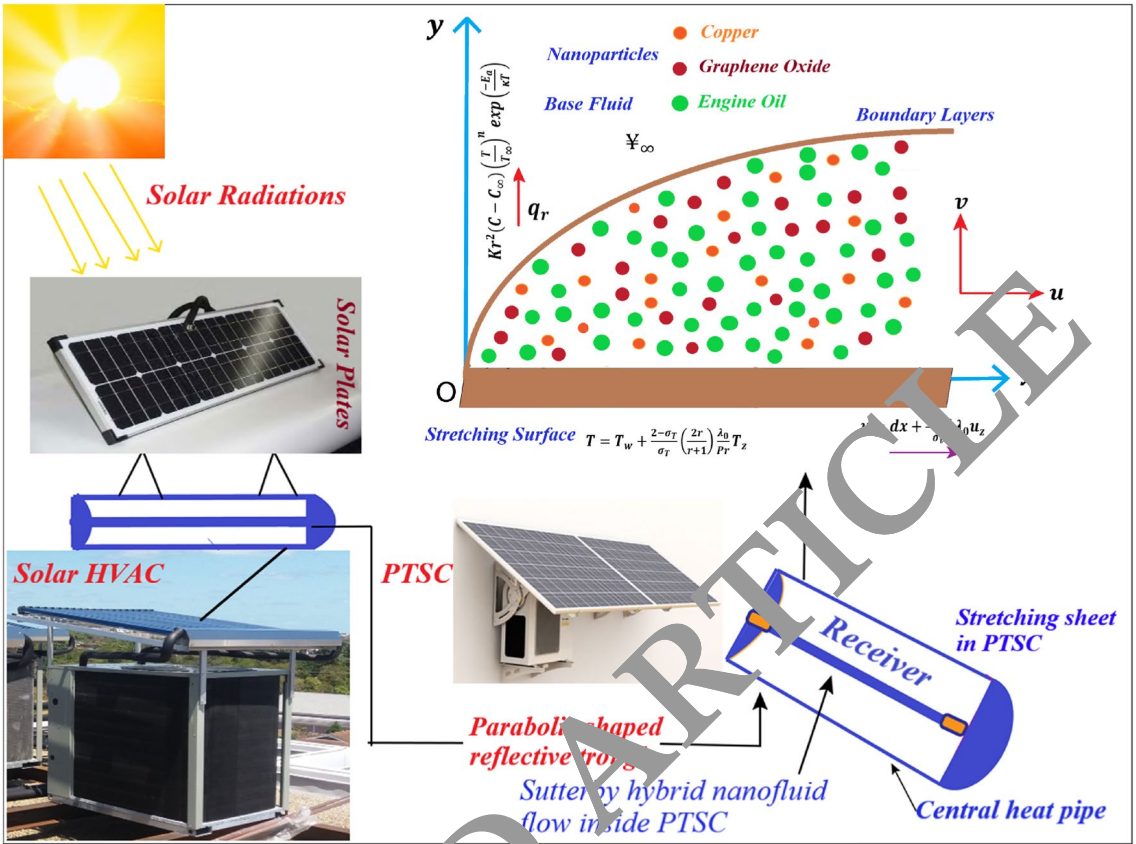

Figure 1. The graphical model of the current problem.

- The effect of ultrafine strong nanoparticles (copper and graphene oxide) at the Sutterby hybrid fluid has yet to be contemplated.
- In the extant literature, no 3D kind of Sutterby nanofluid has been built and explored.
- The results of Maxwell speed slippery and Smoluchowski heat slippery bounder situations on hybrid nanofluid impacting on an extensible floor are but to be investigated.

The paper's structure

The following is a summary of the paper's structure.

- The governing model was created on the premise of a boundary layer.
- The controlling PDEs are converted into ODEs using appropriate similarity transformation.
- The ODEs are adapted to 1st-ordered and resolved a usage of the Keller container numerical method included in MATLAB.
- Physical portions along with the pores and drag force factor and Nusselt number are mathematically decided and demonstrated in tables.
- Mathematical model's velocity, temperature, and awareness elements are numerically calculated and represented withinside the shape of figures.

Proposed mathematical model. The graphical model is presented in Fig. 1, and the characteristics of the proposed mathematical model are as below:

- 3D model (as in Fig. 2), where x- and y- axes contain planes, where z-axis fluid flow region is at the third axis $z \geq 0$.
- The fluid rotates along z-axis, showing that this axis acts as the axis of rotation for the rotating fluid. This fluid has an angular velocity Ω.
- The involved fluid in this model is incompressible Sutterby fluid, flowing on an extendable surface. This surface is located at xy-plane.
- The Maxwell velocity slip[114] effect is investigated, by adding the component of stretching $u_w = dx$, together with the slip length $\frac{2-\sigma_v}{\sigma_v}\lambda_0 U_z$.
- The Smoluchowski temperature slip[115] is added, by implementing the term $\frac{2-\sigma_T}{\sigma_T}\left(\frac{2r}{r+1}\right)\frac{\lambda_0}{P_r}T_z$.

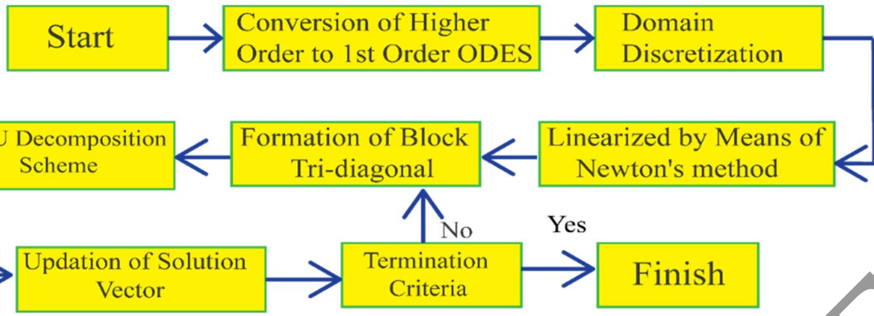

Figure 2. Schematic chat of KBM procedure.

- Surface temperature and concentration are denoted by T_w and C_w, respectively. Meanwhile, T_∞ and C_∞ represent the ambient temperature as well as concentration.

The physical properties of Sutterby hybrid nanofluid are presented in Eq. (1). The dynamics viscosity, density, precise heat and thermal conductivity of hybrid nanofluid are indicated by μ_{hnf}, ρ_{hnf}, α_{hnf}, $(\rho C_p)_{hnf}$ and k_{hnf}, respectively.

$$\left.\begin{aligned} \mu_{hnf} &= \mu_f (1-\phi_{Cu})^{-2.5}(1-\phi_{GO})^{-2.5}, \\ \rho_{hnf} &= \left[(1-\phi_{GO})\left\{(1-\phi_{Cu})\rho_f + \phi_{Cu}\rho_{p_1}\right\}\right] + \phi_{GO}\rho_{p_2}, \\ (\rho C_p)_{hnf} &= [(1-\phi_{GO})\{(1-\phi_{Cu})(\rho C_p)_f + \phi_{Cu}(\rho C_p)_{p_1}\}] + \phi_{GO}(\rho C_p)_{p_2} \\ \frac{\kappa_{hnf}}{\kappa_{gf}} &= \left[\frac{(\kappa_{p_2}+2\kappa_{gf})-2\phi_{GO}(\kappa_{gf}-\kappa_{p_2})}{(\kappa_{p_2}+2\kappa_{gf})+\phi_{GO}(\kappa_{gf}-\kappa_{p_2})}\right]; \frac{\kappa_{gf}}{\kappa_f} = \left[\frac{(\kappa_{p_1}+2\kappa_f)-2\phi_{Cu}(\kappa_f-\kappa_{p_1})}{(\kappa_{p_1}+2\kappa_f)+\phi_{Cu}(\kappa_f-\kappa_{p_1})}\right]. \end{aligned}\right\} \tag{1}$$

A Cauchy tensor of tension for Sutterby liquid is presented as[116]

$$T = -\mathrm{p}I + S, \tag{2}$$

in which p, I and S constitute pressure, identification tensor, and further strain tensor, respectively. Subsequently, S in Eq. (2) is given as

$$S = \mu_0 \left[\frac{sinh^{-1}(E\dot{\gamma})}{E\dot{\gamma}}\right]^m A_1, \tag{3}$$

where in μ_0 is 0 shear fee viscosity, and E is a material time constant. In Eq. (3), the second one invariant stress tensor $\dot{\gamma}$ and primary order Rivilian-Erikson tensor A_1 were interpreted in Eqs. (4) and (5), respectively.

$$\dot{\gamma} = \sqrt{\frac{tr(A_1)^2}{2}}, \tag{4}$$

$$A_1 = (gradV) + (gradV)^T. \tag{5}$$

The m values determine the fluid categories, where Newtonian fluid when $m = 0$, pseudo-plastic (shear thinning) when $m > 0$, and dilatant (shear thickening) when $m < 0$. In addition, the velocity field of the fluid is taken as $V = [u(x,y,z), v(x,y,z), w(x,y,z)]$.

Under the restriction as stated above, the modeled equations are premeditated by[117]:

$$uu_x + vu_y + wu_z = 0, \tag{6}$$

$$uu_x + vu_y + wu_z - 2\Omega v = \frac{\mu_{hnf}}{\rho_{hnf}}\frac{\nu}{2}u_{zz}\left(1 - \frac{Ne^2}{2}(u_z)^2\right), \tag{7}$$

$$uv_x + vv_y + wv_z + 2\Omega u = \frac{\mu_{hnf}}{\rho_{hnf}}\frac{\nu}{2}v_{zz}\left(1 - \frac{Ne^2}{2}(v_z)^2\right), \tag{8}$$

$$uT_x + vT_y + wT_z = \alpha_{hnf}T_{zz} - \frac{1}{(\rho c_p)_{hnf}}(\boldsymbol{q_r})_z, \tag{9}$$

$$uC_x + vC_y + wC_z = DC_{zz} - Kr^2(C - C_\infty)\left(\frac{T}{T_\infty}\right)^n exp\left(\frac{-E_a}{\kappa T}\right). \tag{10}$$

Equations (6)–(10) are controlled by the following boundary conditions:

$$\left.\begin{array}{l} y = 0 : u = dx + \frac{2-\sigma_v}{\sigma_v}\lambda_0 u_z, v = 0, w = 0, C = C_w, \\ T = T_w + \frac{2-\sigma_T}{\sigma_T}\left(\frac{2r}{r+1}\right)\frac{\lambda_0}{Pr}T_z. \\ y \to \infty : u \to 0, v \to 0, T \to T_\infty, C \to C_\infty. \end{array}\right\} \tag{11}$$

In Eq. (9), Rosseland approximation[118] is added:

$$q_r = -\frac{4\sigma^*}{3\kappa^*}T_z^4 = -\frac{4\sigma^*}{3\kappa^*}T^3\frac{\partial^2 T}{\partial z}. \tag{12}$$

where in σ^* and κ^* stand for Stefan-Boltzmann consistent and imply absorption coefficient, respectively.

The appropriate transformations[119] have been selected, as shown in (13):

$$\left.\begin{array}{l} u = dxf'(\beta), \quad v = dxg(\beta), \quad w = -\sqrt{dv}f(\beta), \quad \theta(\beta) = \frac{T-T_\infty}{T_w-T_\infty}, \\ \beta = \sqrt{\frac{d}{\nu}}z, \quad \phi(\beta) = \frac{C-C_\infty}{C_w-C_\infty}. \end{array}\right\} \tag{13}$$

The transformations (13) are implemented to dimensionless the early mathematical model (6)–(10), together with (12). As a result, the following forms have occurred:

$$f'''\left(1 - \frac{N}{2}R_\eta D_\eta f''^2\right) - 2B_1B_2f'^2 + 2B_1B_2ff'' + 4B_1B_2\lambda g = 0, \tag{14}$$

$$g''\left(1 - \frac{N}{2}R_\eta D_\eta f'^2\right) - 2B_1B_2f'g + 2B_1B_2fg' - 4B_1B_2\lambda f' = 0, \tag{15}$$

$$\left(B_3 + \frac{4}{3}R_\delta\right)\theta'' + B_4P_rf\theta' = 0, \tag{16}$$

$$\phi'' + S_\delta f\phi' - \sigma S_\delta(1 + \Gamma\theta)^n exp\left(\frac{-E}{1 + \Gamma\theta}\right)\phi = 0, \tag{17}$$

After implementing (13) in (11), the dimensionless BCs are:

$$\left.\begin{array}{c} \beta \to 0 : f'(0) = 1 + \Gamma_1 f''(0), \quad g(0) = 0, \quad f(0) = 0, \quad \theta(0) = 1 + \Gamma_2\theta', \quad \phi' = 1. \\ \beta \to \infty : f' \to 0, \quad g \to 0, \quad \theta \to 0, \quad \phi \to 0. \end{array}\right\} \tag{18}$$

The final dimensionless governing parameters in (14)–(17) have been derived as

$$\left.\begin{array}{l} E = \left(\frac{E_a}{\kappa T_\infty}\right), \Gamma = \frac{T_w - T_\infty}{T_\infty}, R_\eta = \frac{dx^2}{\nu}, D_\eta = e^2d^2, S_\delta = \frac{\nu}{D}, \\ \sigma = \frac{k_r^2}{a}, \lambda = \frac{\Omega}{d}, \Gamma_1 = \frac{2-\sigma_v}{\sigma_v}\lambda_0\sqrt{\frac{d}{\nu}}, \Gamma_2 = \frac{2-\sigma_T}{\sigma_T}\frac{\lambda_0}{Pr}\frac{2r}{r+1}\sqrt{\frac{d}{\nu}}, \\ R_\delta = \frac{4\sigma T_\infty^3}{k^* k_\infty} \end{array}\right\} \tag{19}$$

where B_1, B_2, B_3 and B_4 are constants[120] as below:

$$\left.\begin{array}{l} B_1 = \frac{1}{(1-\phi_{Cu})^{2.5}(1-\phi_{GO})^{2.5}}, \\ B_2 = \frac{1}{(1-\phi_{GO})\{(1-\phi_{Cu})+\phi_1\frac{\rho_{p1}}{\rho_f}\}+\phi_{GO}\frac{\rho_{p2}}{\rho_f}}, \\ B_3 = \left[\frac{(\kappa_{p_2}+2\kappa_{gf})-2\phi_{GO}(\kappa_{gf}-\kappa_{p_2})}{(\kappa_{p_2}+2\kappa_{gf})+\phi_{GO}(\kappa_{gf}-\kappa_{p_2})}\right]\left[\frac{(\kappa_{p_1}+2\kappa_f)+\phi_{Cu}(\kappa_f-\kappa_{p_1})}{(\kappa_{p_1}+2\kappa_f)-2\phi_{Cu}(\kappa_f-\kappa_{p_1})}\right], \\ B_4 = (1 - \phi_{GO})\{(1 - \phi_{Cu}) + \phi_{Cu}\frac{(\rho C_p)_{p_1}}{(\rho C_p)_f}\} + \phi_{GO}\frac{(\rho C_p)_{p_2}}{(\rho C_p)_f}. \end{array}\right\} \tag{20}$$

Thermophysical properties of copper and graphene oxide nanoparticles[120,121] have been tabulated in Table 1.

The skin friction coefficients in horizontal x- and vertical axes y- are shown in Eq. (21). From Eq. (21) also, τ_{xz} and τ_{yz}[122] are expressed in Eq. (22).

$$Cf_x = \frac{\tau_{xz}}{\rho_f U_w^2}, \quad Cf_y = \frac{\tau_{yz}}{\rho_f U_w^2}, \tag{21}$$

$$\tau_{xz} = -\mu_{hnf}\left[u_z + \frac{Ne^2}{3}(u_z)^3\right], \quad \tau_{yz} = -\mu_{hnf}\left[v_z + \frac{Ne^2}{3}(v_z)^3\right], \tag{22}$$

Thermophysical	ρ (kg/m^3)	c_p (J/kgK)	k (W/mK)
Copper (Cu)	8933	385.0	401.00
Engine oil (EO)	884	1910	0.144
Graphene oxide (GO)	1800	717	5000

Table 1. Thermophysical properties.

Finally, surface drag coefficients are derived as:

$$Cf_x Re_x^{1/2} = \frac{f'' + \frac{N}{3}R_\eta D_\eta f''^3}{B_1}, \quad Cf_y Re_x^{1/2} = \frac{g' + \frac{N}{3}R_\eta D_\eta g'^3}{B_1}. \tag{23}$$

The dimensional heat transfer coefficient[122] is expressed in Eq. (24), where the heat flux q_w is shown in Eq. (25).

$$Nu_x = \frac{xq_w}{(T_f - T_\infty)}\bigg|_{z=0} + \frac{xq_r}{k(T_f - T_\infty)}\bigg|_{z=0}, \tag{24}$$

$$q_w = -k\,T_z|_{z=0}. \tag{25}$$

From Eqs. (24), (25), the dimensionless Nusselt number is obtained:

$$Nu_x Re_x^{-1/2} = -\left(B_3 + \frac{4}{3}R_\delta\right)\theta'(0). \tag{26}$$

The Sherwood number and the mass flux are given in Eqs. (27) and (28), respectively.

$$Sh_x = \frac{xj_w}{D(C_w - C_\infty)}C_z|_{z=0}, \tag{27}$$

$$j_w = -D\,C_z|_{z=0}, \tag{28}$$

After manipulation of Eq. (28) into Eq. (27), The dimensionless shape of the mass transfer coefficient is

$$Sh_x Re_x^{-1/2} = -\phi'(0). \tag{29}$$

Numerical scheme

Keller box method (KBM)[123] is selected as the current numerical technique to perform the solutions for the ODEs (14)–(17), together with BCs (18). The coding of KBM is built in MATLAB software, wherein the flow chart of KBM technique is depicted in Fig. 2. The present-day numerical method applies a finite distinction scheme, which is a collocation technique of order 4 and it runs in the back of KBM MATLAB. The above-mentioned nonlinear differential problem, i.e., Eqs. (14)–(17) followed by the end point condition supplied by Eq. (18) is solved using the Keller box approach.

Step 1 Conversion of ODEs

The aforementioned equations are fairly turned into a new sophisticated first order coupled system:

$$\left.\begin{array}{ll}
y_1' = y_2, & y_1(0) = 0, \\
y_2' = y_3, & y_2(0) = 1 + \Gamma_1 s, \\
y_3' = \frac{2B_1B_2[y_2 - 2\lambda y_4 - y_1y_3]}{1 - \frac{N}{2}R_\eta D_\eta y_3^2}, & y_3(0) = s, \\
y_4' = y_5, & y_4(0) = 0, \\
y_5' = \frac{2B_1B_2[2\lambda y_2 - y_1y_5 + y_4y_2]}{1 - \frac{N}{2}R_\eta D_\eta y_5^2}, & y_5(0) = t, \\
y_6' = y_7, & y_6(0) = 1 + \Gamma_2 u, \\
y_7' = \frac{P_r fb_4 y_1 y_7}{\left(B_3 + \frac{4}{3}R_\delta\right)}, & y_7(0) = u, \\
y_8' = y_9, & y_8(0) = 1, \\
y_9' = \left(\sigma S_\delta(1 + \Gamma y_6)^n exp\left(\frac{-E}{1+\Gamma y_6}\right)\right)y_9 - S_\delta y_1 y_9, & y_9(0) = v.
\end{array}\right\} \tag{30}$$

Step 2 Domain discretization & difference equations

Likewise, domain discretization in $x-\beta$ plane is signified. In view of this web, net points are $\beta_0=0, \beta_j=\beta_{j-1}+h_j, j=0,1,2,3...,J, \beta_J=1$ where, h_j is the step-size. Relating central difference formulation at midpoint $\beta_{j-1/2}$

$$\left(\frac{(y_1)_j-(y_1)_{j-1}}{h_j}\right)=\left(\frac{(y_2)_j+(y_2)_{j-1}}{2}\right), \tag{31}$$

$$\left(\frac{(y_2)_j-(y_2)_{j-1}}{h_j}\right)=\left(\frac{(y_3)_j+(y_3)_{j-1}}{2}\right), \tag{32}$$

$$\left(\frac{(y_4)_j-(y_4)_{j-1}}{h_j}\right)=\left(\frac{(y_5)_j+(y_5)_{j-1}}{2}\right), \tag{33}$$

$$\left(\frac{(y_6)_j-(y_6)_{j-1}}{h_j}\right)=\left(\frac{(y_7)_j+(y_7)_{j-1}}{2}\right), \tag{34}$$

$$\left(\frac{(y_8)_j-(y_8)_{j-1}}{h_j}\right)=\left(\frac{(y_9)_j+(y_9)_{j-1}}{2}\right), \tag{35}$$

$$\left.\begin{array}{c}\left(1-\frac{N}{2}R_\eta D_\eta\left(\frac{(y_3)_j+(y_3)_{j-1}}{2}\right)^2\right)\left(\frac{(y_3)_j-(y_3)_{j-1}}{h_j}\right)-2B_1B_2\left(\frac{(y_2)_j+(y_2)_{j-1}}{2}\right)\\ -2B_1B_2\left[-2\lambda\left(\frac{(y_4)_j+(y_4)_{j-1}}{2}\right)-\left(\frac{(y_1)_j+(y_1)_{j-1}}{2}\right)\left(\frac{(y_3)_j+(y_3)_{j-1}}{2}\right)\right]=0\end{array}\right\} \tag{36}$$

$$\left.\begin{array}{c}\left(1-\frac{N}{2}R_\eta D_\eta\left(\frac{(y_5)_j+(y_5)_{j-1}}{2}\right)^2\right)\left(\frac{(y_5)_j-(y_5)_{j-1}}{h_j}\right)-4B_1B_2\lambda\left(\frac{(y_2)_j+(y_2)_{j-1}}{2}\right)\\ -2B_1B_2\left[-\left(\frac{(y_1)_j+(y_1)_{j-1}}{2}\right)\left(\frac{(y_5)_j+(y_5)_{j-1}}{2}\right)+\left(\frac{(y_4)_j+(y_4)_{j-1}}{2}\right)\left(\frac{(y_2)_j+(y_2)_{j-1}}{2}\right)\right]=0\end{array}\right\} \tag{37}$$

$$\left.\left(B_3+\frac{4}{3}R_\delta\right)\left(\frac{(y_7)_j-(y_7)_{j-1}}{h_j}\right)+P_rfb_4\left(\frac{(y_1)_j+(y_1)_{j-1}}{2}\right)\left(\frac{(y_7)_j+(y_7)_{j-1}}{2}\right)=0\right\} \tag{38}$$

$$\left.\begin{array}{c}\left(\frac{(y_9)_j-(y_9)_{j-1}}{h_j}\right)+S_\delta\left(\frac{(y_1)_j+(y_1)_{j-1}}{2}\right)\left(\frac{(y_9)_j+(y_9)_{j-1}}{2}\right)\\ -\sigma S_\delta\left(1+\Gamma\left(\frac{(y_6)_j+(y_6)_{j-1}}{2}\right)\right)^n\left(1-E\left(1-\Gamma\left(\frac{(6)_j+(y_6)_{j-1}}{2}\right)\right)\right)\left(\frac{(y_9)_j+(y_9)_{j-1}}{2}\right)=0\end{array}\right\}. \tag{39}$$

Step 3 Newton's method

Equations (29) through (37) are linearized using Newton's linearization technique

$$\left.\begin{array}{c}(y_1)_j^{n+1}=(y_1)_j^n+(\delta y_1)_j^n,(y_2)_j^{n+1}=(y_2)_j^n+(\delta y_2)_j^n,\\ (y_3)_j^{n+1}=(y_3)_j^n+(\delta y_3)_j^n,(y_4)_j^{n+1}=(y_4)_j^n+(\delta y_4)_j^n,\\ (y_5)_j^{n+1}=(y_5)_j^n+(\delta y_5)_j^n,(y_6)_j^{n+1}=(y_6)_j^n+(\delta y_6)_j^n,\\ (y_7)_j^{n+1}=(y_7)_j^n+(\delta y_7)_j^n,(y_8)_j^{n+1}=(y_8)_j^n+(\delta y_8)_j^n,\\ (y_9)_j^{n+1}=(y_9)_j^n+(\delta y_9)_j^n.\end{array}\right\} \tag{40}$$

Step 4 Block tridiagonal structure

The linear mathematical model now has the block tridiagonal shape, written

$$A\Delta=S, \tag{41}$$

where

	$-f''(0)$		
λ	Ref.[124]	Ref.[117]	Present results
0.2	– 1.0331	– 1.0330	– 1.0330
0.4	– 1.1009	– 1.1009	– 1.1009
0.5	– 1.1384	– 1.1384	– 1.1384
0.6	– 1.1764	– 1.1763	– 1.1763

Table 2. Assessment of $-f''(0)$ with[117,124].

N	R_η	D_η	λ	Γ_1	$Cf_xRe_x^{\frac{1}{2}}$	$Cf_yRe_x^{\frac{1}{2}}$
0.5	0.5	0.5	0.1	0.5	– 1.57353	– 0.32626
1.0					– 1.72214	– 0.32554
2.0					– 1.80911	– 0.33423
	1.0				– 1.72314	– 0.33522
	1.5				– 1.79635	– 0.33434
	2.0				– 1.80135	– 0.33312
		1.0			– 1.73416	– 0.33432
		3.0			– 2.03212	– 0.33122
		5.0			– 2.42080	– 0.33075
			0.3		– 1.76581	– 0.81728
			0.5		– 1.86153	– 1.17724
			0.7		– 1.95245	– 1.39521
				0.7	– 1.35680	– 0.31952
				0.9	– 1.12517	– 0.28862
				1.1	– 0.97046	– 0.[illegible]68

Table 3. Behaviors of diverse factors on the wall frictional factors.

$$A = \begin{bmatrix} [L_1] & [N_1] & & & & \\ & [L_2] & [N_2] & & & \\ & & \ddots & & & \\ & & \ddots & & & \\ & & \ddots & & & \\ & & & [M_{J-1}] & [L_{J-1}] & [N_{J-1}] \\ & & & & [M_J] & [L_J] \end{bmatrix}, \quad \Delta = \begin{bmatrix} [\Delta_1] \\ \vdots \\ \vdots \\ \vdots \\ [\Delta_{J-1}] \\ [\Delta_J] \end{bmatrix} \text{ and } S = \begin{bmatrix} [S_1] \\ \vdots \\ \vdots \\ \vdots \\ [S_{J-1}] \\ [S_J] \end{bmatrix}. \tag{42}$$

where the overall size of the block-triangle matrix A is J × J and the supervector's block size is 9 × 9. LU decomposition method implementation for solving Δ. A mesh size of h j = 0.01 is regarded adequate for mathematical assessment, and the difference between the current and previous iterations for the needed precision has been set at 10^{-6}.

Result's verification

The comparative analysis of the numerical values skin friction coefficient values $-f''(0)$, are tabulated in Table 2. The comparison is made with the previous researchers[117,124], with the various values of rotating parameter λ. However, other parameters have remained zero such as consistency parameter, Reynolds, Deborah numbers, and speed slippery ($N = R_\eta = D_\eta = \Gamma_1 = 0$). Besides, $B_1 = B_2$ is fixed to obtain this comparative analysis. From Table 2, it is clear that the accuracy of the current results is quite high. Therefore, the current numerical scheme KBS is quite reliable, authentic, and acceptable for subsequent calculations.

Result and discussion

This segment shows and discusses the impact of diverse parameters at the floor frictional factor, Nusselt value, speed, energy, and concentricity outlines with the use of tables and figures. In the case of separated boundaries, Table 3 is intended to mirror the effect of wall frictional factors Cf_x and Cf_y consistent with the table, changes inside the power-regulation conduct list N, Reynolds number R_η, Deborah D_η, pivot boundary and speed slippage cause a decline inside the surface coefficient of drag along the $x-$ orientation, however an expansion when the speed slippage boundary δ_1 is gotten to the next level. This is physically since both the Reynolds number

R_δ	P_r	Γ_2	σ	S_δ	δ	E	n	$Nu_x Re_x^{\frac{-1}{2}}$	$Sh_x Re_x^{\frac{-1}{2}}$
0.5	6450	0.5	0.7	0.7	0.5	0.5	0.5	1.98441	0.75801
1.0								2.04137	0.77854
2.0								2.15052	0.78670
	6.3							1.95437	0.70766
	6.5							1.99442	0.72530
	6.7							2.04212	0.74416
		0.7						1.77233	0.79807
		0.9						1.69735	0.77125
		1.1						1.62549	0.73238
			0.9					1.88597	0.85053
			1.1					1.88597	0.96349
			1.3					1.88597	0.99955
				0.9				1.88597	0.89820
				1.1				1.88597	0.95739
				1.3				1.88597	1.06865
					0.7			1.88597	0.82853
					0.9			1.88597	0.88564
					1.1			1.88597	0.92008
						0.7		1.88597	0.65371
						0.9		1.88597	[illegible]
						1.1		1.88597	[illegible]
							− 0.5	1.88597	[illegible]
							0	[illegible]	0.76627
							0.9	[illegible]	[illegible]

Table 4. Diverse factors influence on Nusselt and Sherwood numbers.

$R_\eta = \frac{dx^2}{\nu}$ and the Deborah number $D_\eta = \frac{a^2 d^2}{\nu}$ depend on the viscosity of the nanofluid and follows the frictional force is diminished. Cf_y ascends because of expansions in N, and Γ_1 but falls in light of an increment in its values. This is because increasing the rapidity slippage $\Gamma_1 = \frac{2-\sigma_v}{\sigma_v}\lambda_0\sqrt{\frac{d}{v}}$ increases the reaction rate, and this effect occurs. Table 4 is expected to examine hotness and mass exchange rates for dimensionless various variables. It is found that when the radiation boundary R_δ and Prandtl number P_r are changed, Nusselt number improves, however, devalues as the temperature slips Γ_2. This is because the presence of heat radiation boosts the stored thermal energy and then begins to release it through the nanofluid molecules, which improves the rate of mutual rate of heat transfer, which in turn grows the number of Nusselt. The mass exchange rate increments when R_δ, substance response rate, Schmidt number Sc, temperature contrast boundary, and fixed value steady n increment, yet reduces as P_r, heat slippery Γ_2, and enactment energy E decline.

The impact of R_η on $f'(\eta)$ is portrayed in Fig. 3. R_η decides if the conduct is laminar or tempestuous at the actual level. The Reynolds number is the ratio of inertial power to gooey power. It is worth noting that the higher the Reynolds number, the greater the inertial power over the gooey power, the thicker the consistency, and the smaller the motion field. Indeed, increasing the volume fraction of nanoparticles reduces liquid fixation, diminishes liquid thickness, and boosts idleness. Finally, a significant component in the lowering of the rapidity field. Figure 4 shows the impact of D_η on $f'(\beta)$. Physically, smaller Deborah values make the material to operate more freely, resulting in a flow of Newtonian viscidity. With increasing Deborah quantities, the effectual enters the non-Newtonianism zone, with increased elasticity ratings and solid-like behavior. The bigger the Deborah quantity, the stronger the viscidness effect. Deborah values distinguish amongst liquid solids and fluid properties on a physical level. As D_η increases, the fluid changes from a fluid to a solid. The substance behaves like a liquid for lesser D_η and such as a solid for greater D_η. As D_η increases, fluid behaviour such as shear thickening becomes more difficult to flow through the surface, lowering $f'(\beta)$. The behavior of the power law exponent M at $f'(\beta)$ (Fig. 5). When shear force is applied, N affects the viscidity of the nanofluid. The letters N stand for fluid shear thinning and Newtonianism. Positive variations in N boost viscidness (shearing thicker) and decrease the velocity of fluid flowing through a ductile surface, thus use caution. Physically, shearing thicker occurs as a result of a larger volume fraction of nanomolecules, a rise in fluid viscosity, and a reduction in fluid rapidity $f'(\beta)$. The relationship between rotational parameter and $f'(\beta)$ is shown in Fig. 6. The fractional size of gold nanomolecules is magnified, which reduces $f'(\beta)$ and the thickness of the momentum boundary layer. An alteration in $f'(\beta)$, acts like shear thickening. When the torque increases, this cause to incremental changes in the viscosity of the fluid to develop, the nanofluid rapidity decreases. The effect of R_η on $g(\beta)$ is depicted in Fig. 7. In opposite of the viscidness influence, R_η emphasizes the relevance of the inertia effect. The consistency of the liquid is decreased, and the liquid speed $g(\beta)$ is diminished when R_η is expanded. The motivation behind Fig. 8 is to stress the feature of D_η on $g(\beta)$. Higher thick powers that lull the liquid speed led to an expansion in D_η. The liquid behaves exactly

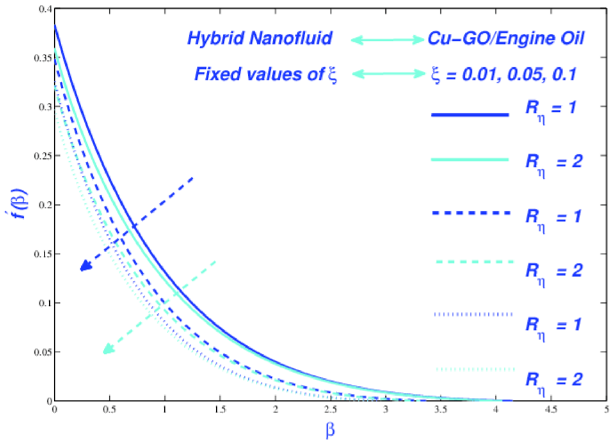

Figure 3. Influence of R_η on f'.

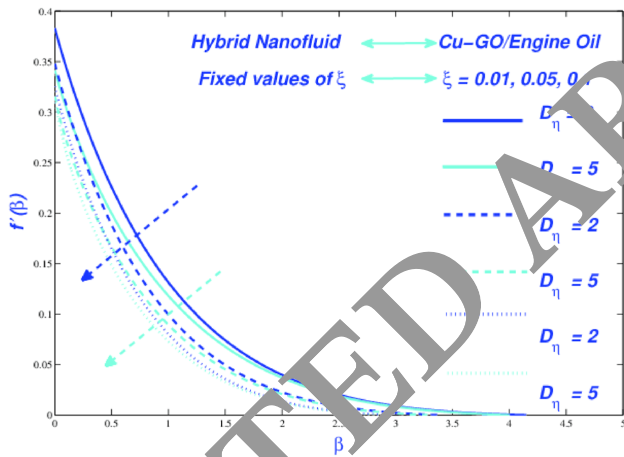

Figure 4. Impact of D_η on f'.

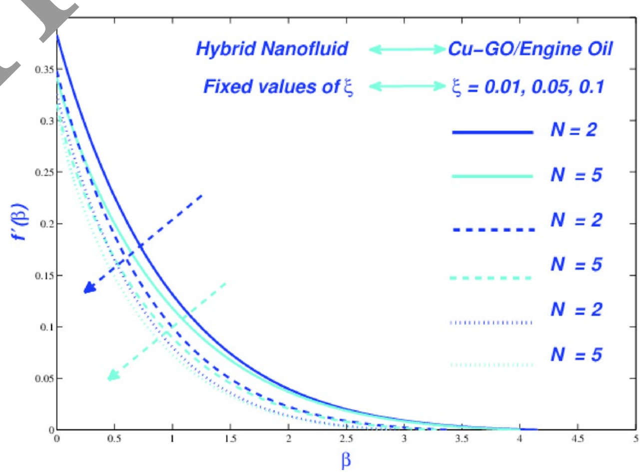

Figure 5. Impact of N on f'.

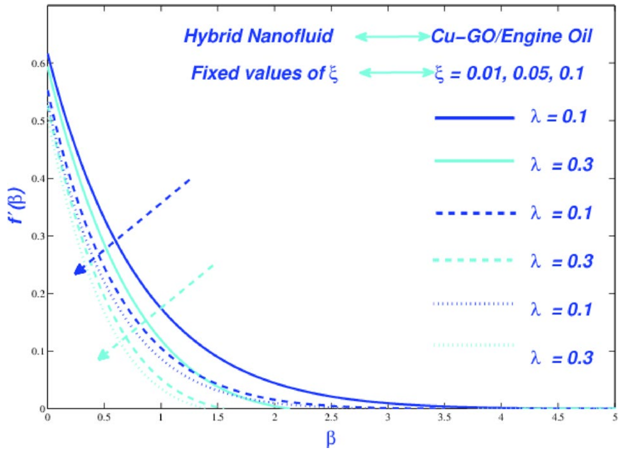

Figure 6. Effect of λ on f'.

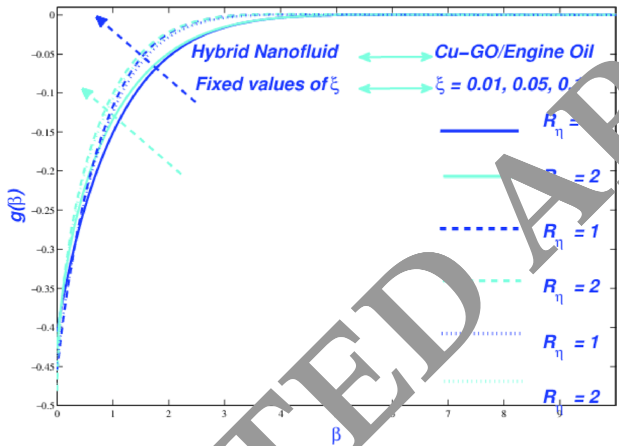

Figure 7. Impact of R_η on g.

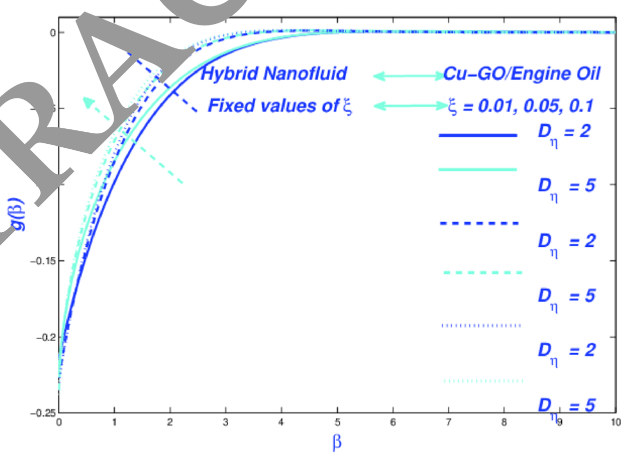

Figure 8. Effect of D_η on f'.

like shearing dilatation due to a consistent change in D_η. It's intriguing to see how increasing the quantity of nanomolecules influences liquid thickness while lowering it. Physically, boosting the amount of nanostructure particles enhances liquid consistency, lowering liquid speed and $g(\beta)$. Figure 9 shows the impact of Γ_1 on $f'(\beta)$. An amplification of Γ_1 lessens the worth of $f'(\beta)$. In the status of slippery limit restrictions, the speed of the plate and the liquid are not equivalent at the plate, bringing about a decrease in liquid speed and a diminishing

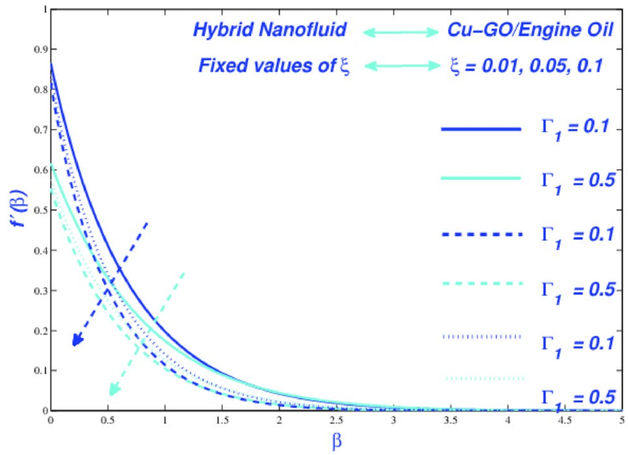

Figure 9. Effect of Γ_1 on f'.

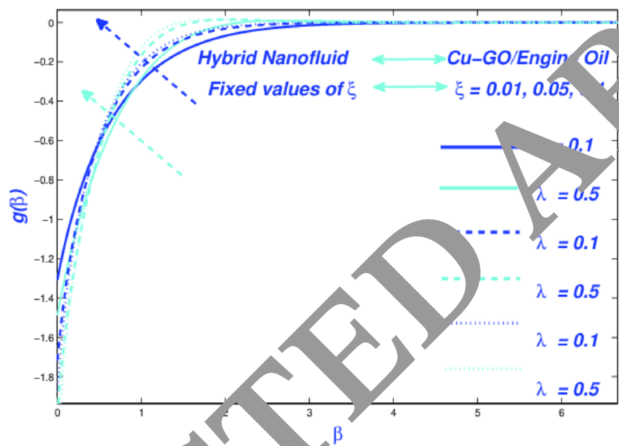

Figure 10. Impact of λ on g.

speed. Figure 10 shows a portrayal of $g(\beta)$. This is physically because the liquid near the boundary layer is more viscous due to the accumulation of particles close to the surface, which reduces the velocity and increases the further away from the boundary layer. Another important concept is that as the percentage of nanoparticles in the nanoliquid grows, the thickness of the liquid reduces, making it simpler to travel across an extensible plate. Magnification in the volume part of nanomolecules builds a liquid and diminishes the liquid speed and $g(\beta)$.

Figure 11 is intended to depict R_δ performing on $\theta(\beta)$. R_δ is the most thing of a heat transfer rules in terms of physics. It is commonly known that amplification in R_δ causes the heat transfer rate to increase. It is because of an improvement in R_δ lowers the average absorbing factor, resulting in amplification in $\theta(\beta)$. Practically, an increase in the size of the nanomolecules paired with R_δ enhances the thermal conducting of the fluid, boosting $\theta(\beta)$. The effect of P_r on $\theta(\beta)$ is depicted in Fig. 12. When P_r is small, heat diffuses quickly in comparison to velocity (momentum), and vice versa when P_r is large. Furthermore, because of amplification in P_r, the thickness of the thermal boundary layer declines $\theta(\beta)$. This is physically due to the inverse relationship between the Prandtl number and the thermal diffusivity, as the lack of thermal diffusivity occurs as a result of the low thermal conducting and thus enhances the Prandtl number, which works to increase the temperature inside the nanoliquid. The link between Γ_1 and temperature is seen in Fig. 13. A magnification of Γ_1 reduces the space among the surface and surrounding heat, transporting less temperature from a plate to a liquid and, due to the lowering a fluid heat.

Figure 14 emphasizes the effect of chemically response charge σ at the awareness area $\phi(\beta)$. The physical interpretation refers to the amount $\sigma(1+\delta\theta)^n exp\left(\frac{-E}{1+\delta\theta}\right)$ magnifies at the likewise of improvement in σ or n which inspires the destructive chemically reactive action which diminishes the mass size range. The exponential part in the formula means that when the active energy diminishes, the rate constant of a reaction grows exponentially. Because the rate of a reaction is directly proportionate to its rate constant, the rate also grows exponentially[125]. The impact of S_δ at the mass area $\phi(\beta)$ is defined in Fig. 15. The Schmidt quantity is the ratio of momentum to mass diffusivity. It's well worth noting that a high-quality alternate in S_δ reduces mass diffusivity.

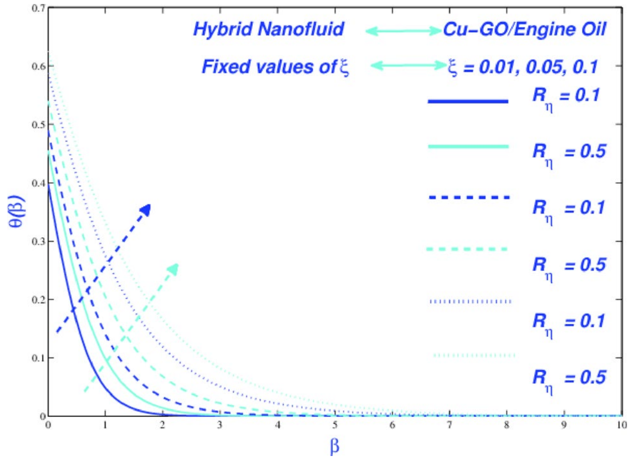

Figure 11. Influence of R_η on θ.

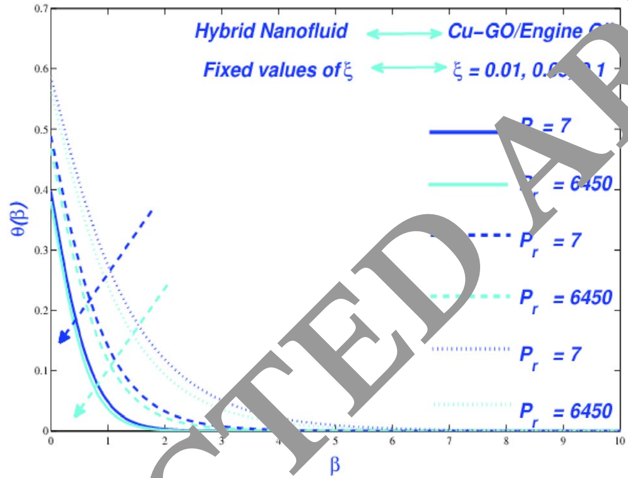

Figure 12. Influence of P_r on θ.

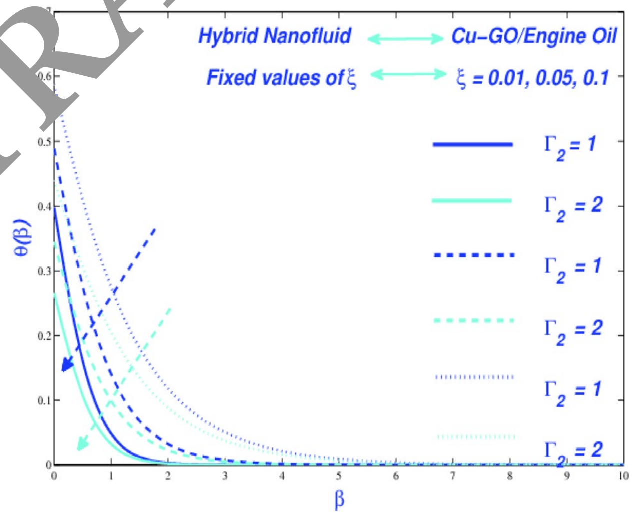

Figure 13. Impact of Γ_2 on θ.

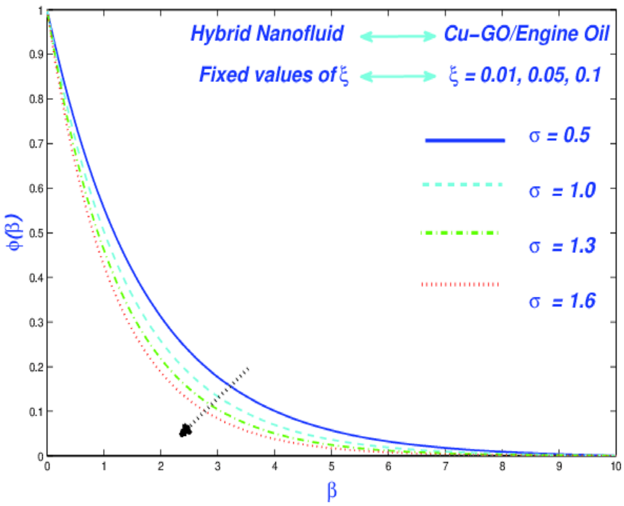

Figure 14. Effect of σ on ϕ.

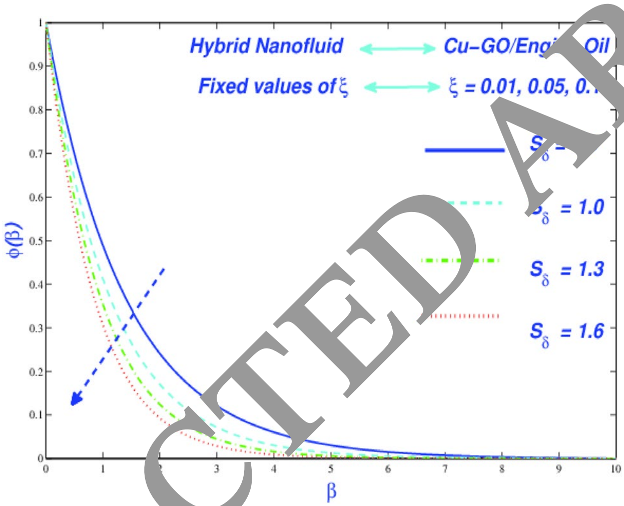

Figure 15. Effect of S_δ on ϕ.

Physically, the fluid viscidness falls because of a growth in $S_\delta = \frac{\nu}{D}$, which reduces mass diffusion and will increase momentum diffusivity. The presence of S_δ maximum possibly reduces the fluid viscidness and $\phi(\beta)$.

Conclusions

3-D rotating Sutterby hybrid fluid with copper-Graphene oxide nanomolecules, active energy, impetus, heat slippery bounder constraints, and radiative heat flow is defined in this paper. The numerical solution to the simulated problem was achieved using the MATLAB KBM built-in technique. The following are some of the most important aspects of the results:

- The profile $f'(\eta)$ denigrates at the behalf of extension in R_η, D_η, and N.
- Magnification withinside the factors λ and N monitors to an extension in $g(\beta)$.
- Intensification in θ_w boosts $\theta(\beta)$ however a decline in $\theta(\beta)$ occurs due to an enhancement in R_δ.
- The value of the Nusselt wide variety decreases below amplification in Γ_1.
- It is essential that $\phi(\beta)$ will increase withinside the case of extension in ξ.
- A positive variant in Γ_2 will increase $\phi(\beta)$.
- The mass fractional size discipline outline reduces for the chemically response factor Γ.

The Keller-box method could be applied to a variety of physical and technical challenges in the future[126–139].

Data availability
The results of this study are available only within the paper to support the data.

Received: 21 March 2022; Accepted: 28 June 2022
Published online: 07 July 2022

References
1. Atiz, A., Karakilcik, H., Erden, M. & Karakilcik, M. Investigation energy, exergy and electricity production performance of an integrated system based on a low-temperature geothermal resource and solar energy. *Energy Convers. Manag.* **195**, 798–809 (2019).
2. Jahangiri, M. *et al.* Using fuzzy MCDM technique to find the best location in Qatar for exploiting wind and solar energy to generate hydrogen and electricity. *Int. J. Hydro. Energy* **45**(27), 13862–13875 (2020).
3. Abban, A. R. & Hasan, M. Z. Solar energy penetration and volatility transmission to electricity markets—An Australian perspective. *Econom. Anal. Policy* **69**, 434–449 (2021).
4. Lazzarin, R. Heat pumps and solar energy: A review with some insights in the future. *Int. J. Refrig.* **116**, 146–16[illegible] (2020).
5. Asfour, S., Bernardin, F. & Toussaint, E. Experimental validation of 2D hydrothermal modelling of porous pavement for heating and solar energy retrieving applications. *Road Mater. Pavem. Design* **21**(3), 666–682 (2020).
6. Heidari, A. & Khovalyg, D. Short-term energy use prediction of solar-assisted water heating system: Application case of combined attention-based LSTM and time-series decomposition. *Sol. Energy* **207**, 626–639 (2020).
7. Pang, W., Yu, H., Zhang, Y. & Yan, H. Solar photovoltaic based air cooling system for vehicles. *Renew. Energy* **130**, 25–31 (2019).
8. Mendecka, B., Cozzolino, R., Leveni, M. & Bella, G. Energetic and exergetic performance evaluation of a solar cooling and heating system assisted with thermal storage. *Energy* **176**, 816–829 (2019).
9. Singh, R. P., Xu, H., Kaushik, S. C., Rakshit, D. & Romagnoli, A. Effective utilization of natural convection via novel fin design and influence of enhanced viscosity due to carbon nanoparticles in a solar cooling thermal storage system. *Sol. Energy* **183**, 105–119 (2019).
10. Kasaeian, A., Rajaee, F. & Yan, W. M. Osmotic desalination by solar energy: A critical review. *Renew. Energy* **134**, 1473–1490 (2019).
11. Santosh, R., Arunkumar, T., Velraj, R. & Kumaresan, G. Technological advancements in solar energy driven humidification-dehumidification desalination systems—A review. *J. Clean. Prod.* [illegible] (2019).
12. Alnaimat, F., Ziauddin, M. & Mathew, B. A review of recent advances in humidification and dehumidification desalination technologies using solar energy. *Desalination* **499**, 114[illegible] (2021).
13. Hernández-Callejo, L., Gallardo-Saavedra, S. & Alonso-Gó[illegible] V. A. A review of photovoltaic systems: Design, operation and maintenance. *Sol. Energy* **188**, 426–440 (2019).
14. Akbari, H. *et al.* Efficient energy storage technologies for photovoltaic systems. *Sol. Energy* **192**, 144–168 (2019).
15. Deschamps, E. M. & Rüther, R. Optimization of inverter loading ratio for grid connected photovoltaic systems. *Sol. Energy* **179**, 106–118 (2019).
16. Cao, Y. *et al.* Towards high efficiency inverted Sb2[illegible]3 thin film solar cells. *Sol. Energy Mater. Sol. Cells* **200**, 109945 (2019).
17. Kowsar, A. *et al.* Progress in major thin-film solar cells: Growth technologies, layer materials and efficiencies. *Int. J. Renew. Energy Res.* **9**(2), 579–597 (2019).
18. Zhao, F. *et al.* The better photoelectric performance of thin-film TiO_2/c-Si heterojunction solar cells based on surface plasmon resonance. *Results Phys.* [illegible], 104[illegible] (2021).
19. Hayat, M. B., Ali, D., Monyake, K. [illegible] Alagha, L. & Ahmed, N. Solar energy—A look into power generation, challenges, and a solar-powered future. *Int. J. Energy Res.* **43**(3), 1049–1067 (2019).
20. Jiménez, P. E. S. *et al.* High performance and low-cost macroporous calcium oxide based materials for thermochemical energy storage in concentrated solar power plants. *Appl. Energy* **235**, 543–552 (2019).
21. Fiuk, J. J. & Dutkowski, K. Experimental investigations on thermal efficiency of a prototype passive solar air collector with wavelike baffles. *Sol. Energy* **188**, 495–506 (2019).
22. Cherier, M. [illegible] *et al.* Energy efficiency and supplement interior comfort with passive solar heating in Saharan climate. *Adv. Build. Energy Res.* **14**[illegible]–114 (2020).
23. Xia, [illegible] J., Ye, Y., Xu, P. & Wang, Y. A real-time monitoring system based on ZigBee and 4G communications for photovoltaic generation. *IEEE J. Power Energy Syst.* **6**(1), 52–63 (2020).
24. Cho, [illegible] *et al.* Application of Photovoltaic Systems for Agriculture: A study on the relationship between power generation and farming for the improvement of photovoltaic applications in agriculture. *Energies* **13**(18), 4815 (2020).
25. Langer, L. & Volling, T. An optimal home energy management system for modulating heat pumps and photovoltaic systems. *Appl. Energy* **278**, 115661 (2020).
26. Sutopo, W., Mardikaningsih, I. S., Zakaria, R. & Ali, A. model to improve the implementation standards of street lighting based on solar energy: A case study. *Energies* **13**(3), 630 (2020).
27. Wassie, Y. T. & Adaramola, M. S. Socio-economic and environmental impacts of rural electrification with solar photovoltaic systems: Evidence from southern Ethiopia. *Energy Sustain. Dev.* **60**, 52–66 (2021).
28. Ali, H. & Khan, H. A. Techno-economic evaluation of two 42 kWp polycrystalline-Si and CIS thin-film based PV rooftop systems in Pakistan. *Renew. Energy* **152**, 347–357 (2020).
29. Suphahitanukool, C. *et al.* An evaluation of economic potential solar photovoltaic farm in Thailand: Case study of polycrystalline silicon and amorphous silicon thin film. *Int. J. Energy Econom. Policy* **8**(4), 33 (2018).
30. Chen, C., Xu, T. B., Yazdani, A. & Sun, J. Q. A high density piezoelectric energy harvesting device from highway traffic—System design and road test. *Appl. Energy* **299**, 117331 (2021).
31. Elsheikh, A. H. *et al.* Thin film technology for solar steam generation: A new dawn. *Sol. Energy* **177**, 561–575 (2019).
32. Lstiburek, J. W. & Eng, P. Mold in alligator alley. *ASHRAE J.* **51**(9), 72 (2009).
33. Alavy, M. & Siegel, J. A. In-situ effectiveness of residential HVAC filters. *Indoor Air* **30**(1), 156–166 (2020).
34. Stopps, H., Huchuk, B., Touchie, M. F. & O'Brien, W. Is anyone home? A critical review of occupant-centric smart HVAC controls implementations in residential buildings. *Build. Environ.* **187**, 107369 (2020).
35. MacDonald, J. S., Vrettos, E. & Callaway, D. S. A critical exploration of the efficiency impacts of demand response from HVAC in commercial buildings. *Proc. IEEE* **108**(9), 1623–1639 (2020).
36. Khalilnejad, A., French, R. H. & Abramson, A. R. Data-driven evaluation of HVAC operation and savings in commercial buildings. *Appl. Energy* **278**, 115505 (2020).
37. Joubert, A., Ali, S. A. Z., Frossard, M. & Andrès, Y. Dust and microbial filtration performance of regular and antimicrobial HVAC filters in realistic conditions. *Environ. Sci. Pollut. Res.* **28**, 39907–39919 (2021).
38. Mahdavi, A. & Siegel, J. A. Extraction of dust collected in HVAC filters for quantitative filter forensics. *Aerosol Sci. Technol.* **54**(11), 1282–1292 (2020).

39. Raman, N. S., Devaprasad, K., Chen, B., Ingley, H. A. & Barooah, P. Model predictive control for energy-efficient HVAC operation with humidity and latent heat considerations. *Appl. Energy* **279**, 115765 (2020).
40. Zhu, H. C., Ren, C. & Cao, S. J. Fast prediction for multi-parameters (concentration, temperature and humidity) of indoor environment towards the online control of HVAC system, In *Building Simulation*, Vol. 14, 3, 649–665 (Tsinghua University Press, 2021).
41. Hollick, J. C. Hollick solar systems Ltd, Method and apparatus for cooling ventilation air for a building, U.S. Patent 8, 827 (2014).
42. Faraz, T. Benefits of concentrating solar power over solar photovoltaic for power generation in Bangladesh, In *2nd International Conference on the Developments in Renewable Energy Technology*, 1–5 (IEEE, 2012).
43. Lamrani, B., Kuznik, F. & Draoui, A. Thermal performance of a coupled solar parabolic trough collector latent heat storage unit for solar water heating in large buildings. *Renew. Energy* **162**, 411–426 (2020).
44. Özcan, A., Devecioğlu, A. G. & Oruç, V. Experimental and numerical analysis of a parabolic trough solar collector for water heating application. *Energy Sourc A Recov. Utili. Environ. Effects* https://doi.org/10.1080/15567036.2021.1924317 (2021).
45. Bi, Y., Qin, L., Guo, J., Li, H. & Zang, G. Performance analysis of solar air conditioning system based on the independent-developed solar parabolic trough collector. *Energy* **196**, 117075 (2020).
46. Ali, D. & Ratismith, W. A semicircular trough solar collector for air-conditioning system using a single effect NH_3-H_2O absorption chiller. *Energy* **215**, 119073 (2021).
47. Shahzad, F. *et al.* Thermal analysis on Darcy-Forchheimer swirling Casson hybrid nanofluid flow inside parallel plates in parabolic trough solar collector: An application to solar aircraft. *Int. J. Energy Res.* **45**, 20812–20834 (2021).
48. Sajid, T. *et al.* Study on heat transfer aspects of solar aircraft wings for the case of Reiner-Philippoff hybrid nanofluid past a parabolic trough: Keller box method. *Phys. Scr.* **96**, 095220 (2021).
49. Sajid, T. *et al.* Entropy analysis and thermal characteristics of Reiner Philippoff hybrid nanofluidic flow via a parabolic trough of solar aircraft wings: Keller box method. *Res. Square* https://doi.org/10.21203/rs.3.rs-7[illegible]495/v1 (2021).
50. Jamshed, W. Thermal augmentation in solar aircraft using tangent hyperbolic hybrid nanofluid: A solar energy application. *Energy Environ.* https://doi.org/10.1177/0958305X211036671 (2021).
51. Jamshed, W., Nisar, K. S., Ibrahim, R. W., Shahzad, F. & Eid, M. R. Thermal expansion optimization in solar aircraft using tangent hyperbolic hybrid nanofluid: A solar thermal application. *J. Mater. Res. Technol.* **14**, 985–1006 (2021).
52. Tagle-Salazar, P. D., Nigam, K. D. & Rivera-Solorio, C. I. Parabolic trough solar collectors: A general overview of technology, industrial applications, energy market, modeling, and standards. *Green Proc. Synth.* **9**(1), 595–649 (2020).
53. Rostami, S., Shahsavar, A., Kefayati, G. & Goldanlou, A. S. Energy and exergy analysis of using turbulator in a parabolic trough solar collector filled with mesoporous silica modified with copper nanoparticles hybrid nanofluid. *Energies* **13**(11), 2946 (2020).
54. Mahani, R. B., Hussein, A. K. & Talebizadehsardari, P. Thermal–hydraulic performance of hybrid nano-additives containing multiwall carbon nanotube-Al_2O_3 inside a parabolic through solar collector with turbulators. *Math. Meth. Appl. Sci.* https://doi.org/10.1002/mma.6842 (2020).
55. Al-Rashed, A. A., Alnaqi, A. A. & Alsarraf, J. Thermo-hydraulic and economic performance of a parabolic trough solar collector equipped with finned rod turbulator and filled with oil-based hybrid nanofluid. *J. Taiwan Inst. Chem. Eng.* **124**, 192–204 (2021).
56. Alnaqi, A. A., Alsarraf, J. & Al-Rashed, A. A. Hydrothermal effects of using two twisted tape inserts in a parabolic trough solar collector filled with MgO-MWCNT/thermal oil hybrid nanofluid. *Sustain. Energy Tech. Assess.* **47**, 101331 (2021).
57. Zaboli, M., Ajarostaghi, S. S. M., Saedodin, S. & Ghorbani, B. Hybrid nanofluid flow and heat transfer in a parabolic trough solar collector with inner helical axial fins as turbulator. *Eur. Phys. J. Plus* **136**(8), 841 (2021).
58. Mohammed, H. A., Vuthaluru, H. B. & Liu, S. Heat transfer augmentation of parabolic trough solar collector receiver's tube using hybrid nanofluids and conical turbulators. *J. Taiwan Inst. Chem. Eng.* **125**, 215–242 (2021).
59. Afridi, M. I., Alkanhal, T. A., Qasim, M. & Tlili, I. Entropy generation in Cu-Al_2O_3-H_2O hybrid nanofluid flow over a curved surface with thermal dissipation. *Entropy* **21**(10), 941 (2019).
60. Alsabery, A. I. *et al.* Entropy generation and natural convection flow of hybrid nanofluids in a partially divided wavy cavity including solid blocks. *Energies* **13**(11), 2942 (2020).
61. Aziz, A., Jamshed, W., Aziz, T., Bahaidarah, H. M. & Rehman, K. U. Entropy analysis of Powell-Eyring hybrid nanofluid including effect of linear thermal radiation and viscous dissipation. *J. Therm. Anal. Calorim.* **143**(2), 1331–1343 (2021).
62. Parveen, N. *et al.* Entropy generation analysis and radiated heat transfer in MHD (Al_2O_3-Cu/water) hybrid nanofluid flow. *Micromachines* **12**(8), 887 (2021).
63. Mumraiz, S., Ali, A., Awais, M., Shutaywi, M. & Shah, Z. Entropy generation in electrical magnetohydrodynamic flow of Al_2O_3–Cu/H_2O hybrid nanofluid with non-uniform heat flux. *J. Therm. Anal. Calorim.* **143**(3), 2135–2148 (2021).
64. Li, Y. X. *et al.* Dynamics of aluminum oxide and copper hybrid nanofluid in nonlinear mixed Marangoni convective flow with entropy generation: Applications to renewable energy. *Chin. J. Phys.* **73**, 275–287 (2021).
65. Ghalambaz, M., Zadeh, S. M. H., Veismoradi, A., Sheremet, M. A. & Pop, I. Free convection heat transfer and entropy generation in an odd-shaped cavity filled with a Cu-Al_2O_3 hybrid nanofluid. *Symmetry* **13**(1), 122 (2021).
66. Das, S., Sarkar, S. & Jana, R. N. Feature of entropy generation in Cu-Al_2O_3/ethylene glycol hybrid nanofluid flow through a rotating channel. *BioNanoSci.* **10**(4), 950–967 (2020).
67. Xia, W. F., Hafeez, M. U., Khan, M. I., Shah, N. A. & Chung, J. D. Entropy optimized dissipative flow of hybrid nanofluid in the presence of nonlinear thermal radiation and Joule heating. *Sci. Rep.* **11**(1), 1–16 (2021).
68. Reddy, P. S. & Sreedevi, P. Entropy generation and heat transfer analysis of magnetic hybrid nanofluid inside a square cavity with thermal radiation. *Eur. Phys. J. Plus* **136**(1), 1–33 (2021).
69. Gokulavani, P., Muthtamilselvan, M. & Abdalla, B. Impact of injection/suction and entropy generation of the porous open cavity with the hybrid nanofluid. *J. Therm. Anal. Calorim.* **147**, 3299–3312 (2021).
70. Gireesha, B. J., Gangadhar, K. & Sindhu, S. Entropy generation analysis of electrical magnetohydrodynamic flow of TiO_2-Cu/H_2O hybrid nanofluid with partial slip. *Int. J. Numer. Meth. Heat Fluid Flow* **31**, 1905–1929 (2021).
71. McCash, L. B., Akhtar, S., Nadeem, S. & Saleem, S. Entropy analysis of the peristaltic flow of hybrid nanofluid inside an elliptic duct with sinusoidally advancing boundaries. *Entropy* **23**(6), 732 (2021).
72. Khan, M. I., Hafeez, M. U., Hayat, T., Khan, M. I. & Alsaedi, A. Magneto rotating flow of hybrid nanofluid with entropy generation. *Comput. Meth. Prog. Biomed.* **183**, 105093 (2020).
73. Sindhu, S. & Gireesha, B. J. Entropy generation analysis of hybrid nanofluid in a microchannel with slip flow, convective boundary and nonlinear heat flux. *Int. J. Numer. Meth. Heat Fluid Flow* **31**, 53–74 (2020).
74. Aziz, A., Jamshed, W., Ali, Y. & Shams, M. Heat transfer and entropy analysis of Maxwell hybrid nanofluid including effects of inclined magnetic field, Joule heating and thermal radiation. *Discr. Contin. Dyn. Syst.-S* **13**(10), 2667 (2020).
75. Munawar, S. & Saleem, N. Entropy generation in thermally radiated hybrid nanofluid through an electroosmotic pump with ohmic heating: Case of synthetic cilia regulated stream. *Sci. Prog.* **104**(3), 368504211025921 (2021).
76. Abu-Libdeh, N. *et al.* Hydrothermal and entropy investigation of Ag/MgO/H_2O hybrid nanofluid natural convection in a novel shape of porous cavity. *Appl. Sci.* **11**(4), 1722 (2021).
77. Samal, S. K. & Moharana, M. K. Thermo-hydraulic and entropy generation analysis of recharging microchannel using water-based graphene–silver hybrid nanofluid. *J. Therm. Anal. Calorim.* **143**(6), 4131–4148 (2021).
78. Jamshed, W. & Aziz, A. Cattaneo-Christov based study of TiO_2–CuO/EG Casson hybrid nanofluid flow over a stretching surface with entropy generation. *Appl. Nanosci.* **8**, 685–698 (2018).

79. Mabood, F., Shafiq, A., Khan, W. A. & Badruddin, I. A. MHD and nonlinear thermal radiation effects on hybrid nanofluid past a wedge with heat source and entropy generation. *Int. J. Numer. Meth. Heat Fluid Flow* **32**, 120–137 (2021).
80. Shah, Z., Sheikholeslami, M., Kumam, P. & Shafee, A. Modeling of entropy optimization for hybrid nanofluid MHD flow through a porous annulus involving variation of Bejan number. *Sci. Rep.* **10**(1), 1–14 (2020).
81. Benzema, M., Benkahla, Y. K., Boudiaf, A., Ouyahia, S. E. & El Ganaoui, M. Entropy generation due to the mixed convection flow of MWCNT–MgO/water hybrid nanofluid in a vented complex shape cavity. In *MATEC Web of Conferences* 307, 01007 (EDP Sciences, 2020).
82. Isa, S. S. P. M. *et al.* MHD mixed convection boundary layer flow of a Casson fluid bounded by permeable shrinking sheet with exponential variation. *Sci. Iran.* **24**(2), 637–647 (2017).
83. Parvin, S., Isa, S. S. P. M., Arifin, N. M. & Ali, F. M. The magnetohydrodynamics Casson fluid flow, heat and mass transfer due to the presence of assisting flow and buoyancy ratio parameters. *CFD Lett.* **12**(8), 64–75 (2020).
84. Parvin, S., Isa, S. S. P. M., Arifin, N. M. & Ali, F. M. Dual numerical solutions on mixed convection Casson fluid flow due to the effect of the rate of extending and compressing sheet—Stability analysis. *CFD Lett.* **12**(8), 76–84 (2020).
85. Farooq, U., Ijaz, M. A., Khan, M. I., Isa, S. S. P. M. & Lu, D. C. Modeling and non-similar analysis for Darcy-Forchheimer-Brinkman model of Casson fluid in a porous media. *Int. Commun. Heat Mass Transf.* **119**, 104955 (2020).
86. Parvin, S., Isa, S. S. P. M., Arifin, N. M. & Ali, F. M. The inclined factors of magnetic field and shrinking sheet in Casson fluid flow, heat and mass transfer. *Symmetry* **13**(3), 373 (2021).
87. Parvin, S., Isa, S. S. P. M., Jamshed, W., Ibrahim, R. W. & Nisar, K. S. Numerical treatment of 2D magneto double-diffusive convection flow of a Maxwell nanofluid: Heat transport case study. *Case Stud. Therm. Eng.* **28**, 101383 (2021).
88. Khan, M. N., Ullah, N. & Nadeem, S. Transient flow of Maxwell nanofluid over a shrinking surface: Numerical solutions and stability analysis. *Surf. Interfaces* **22**, 100829 (2021).
89. Shi, Q. H. *et al.* Dual solution framework for mixed convection flow of Maxwell nanofluid instigated by exponentially shrinking surface with thermal radiation. *Sci. Rep.* **11**(1), 1–12 (2021).
90. Ahmad, F. *et al.* The improved thermal efficiency of Maxwell hybrid nanofluid comprising of graphene oxide plus silver/kerosene oil over stretching sheet. *Case Stud. Therm. Eng.* **27**, 101257 (2021).
91. Saleem, M., Tufail, M. N. & Chaudhry, Q. A. One-parameter scaling transformations of Maxwell nanofluid with Ludwig-Soret and pedesis motion passed over stretching–shrinking surfaces. *Microfluid. Nanofluid.* **25**(3), 1–15 (2021).
92. Sutterby, J. L. Laminar converging flow of dilute polymer solutions in conical sections: Part I. Viscosity data, new viscosity model, tube flow solution. *AIChE J.* **12**(1), 63–68 (1966).
93. Sutterby, J. L. Laminar converging flow of dilute polymer solutions in conical sections. II.. *Trans. Soc. Rheol.* **9**(2), 227–241 (1965).
94. Zhang, X., Duan, X., Muzychka, Y. & Wang, Z. Experimental correlation for pipe flow drag reduction using relaxation time of linear flexible polymers in a dilute solution. *Can. J. Chem. Eng.* **98**(3), 792–803 (2020).
95. Mohammadtabar, M., Sanders, R. S. & Ghaemi, S. Viscoelastic properties of flexible and rigid polymers for turbulent drag reduction. *J. Non-Newtonian Fluid Mech.* **283**, 104347 (2020).
96. Malkin, A. Y., Subbotin, A. V. & Kulichikhin, V. G. Stability of polymer jets in extension: Physicochemical and rheological mechanisms. *Russian Chem. Rev.* **89**(8), 811 (2020).
97. Deshawar, D., Gupta, K. & Chokshi, P. Electrospinning of polymer solutions: An analysis of instability in a thinning jet with solvent evaporation. *Polymer* **202**, 122656 (2020).
98. Scott, A. J., Romero-Zerón, L. & Penlidis, A. Evaluation of polymeric materials for chemical enhanced oil recovery. *Processes* **8**(3), 361 (2020).
99. Rock, A., Hincapie, R. E., Tahir, M., Langanke, N. & Ganzer, L. On the role of polymer viscoelasticity in enhanced oil recovery: Extensive laboratory data and review. *Polymers* **12**(10), 2276 (2020).
100. Sohail, M. *et al.* Computational exploration for radiative flow of Sutterby nanofluid with variable temperature-dependent thermal conductivity and diffusion coefficient. *Open Phys.* **18**(1), 1073–1083 (2020).
101. Raza, R., Sohail, M., Abdeljawad, T., Naz, R. & Thounthong, P. Exploration of temperature-dependent thermal conductivity and diffusion coefficient for thermal and mass transportation in sutterby nanofluid model over a stretching cylinder. *Complexity* **2021**, 6252864 (2021).
102. Waqas, H., Farooq, U., Bhatti, M. M. & Hussain, S. Magnetized bioconvection flow of Sutterby fluid characterized by the suspension of nanoparticles across a wedge with activation energy. *ZAMM J. Appl. Math. Mech.* **101**, e202000349 (2021).
103. Waqas, H., Farooq, U., Muhammad, T., Hussain, S. & Khan, I. Thermal effect on bioconvection flow of Sutterby nanofluid between two rotating disks with motile microorganisms. *Case Stud. Therm. Eng.* **26**, 101136 (2021).
104. Gowda, R. P., Kumar, R. N., Rauf, A., Prasannakumara, B. C. & Shehzad, S. A. Magnetized flow of sutterby nanofluid through cattaneo-christov theory of heat diffusion and stefan blowing condition. *Appl. Nanosci.* **21**, 1–10 (2021).
105. Yahya, A. U. *et al.* Implication of Bio-convection and Cattaneo-Christov heat flux on Williamson Sutterby nanofluid transportation caused by a stretching surface with convective boundary. *Chin. J. Phys.* **73**, 706–718 (2021).
106. Khan, U., Shafiq, A., Zaib, A., Wakif, A. & Baleanu, D. Numerical exploration of MHD falkner-skan-sutterby nanofluid flow by utilizing an advanced non-homogeneous two-phase nanofluid model and non-Fourier heat-flux theory. *Alex. Eng. J.* **59**(6), 4851–4864 (2020).
107. Hayat, T., Nisar, Z., Alsaedi, A. & Ahmad, B. Analysis of activation energy and entropy generation in mixed convective peristaltic transport of Sutterby nanofluid. *J. Therm. Anal. Calorim.* **143**(3), 1867–1880 (2021).
108. El-Dabe, N. T., Moatimid, G. M., Mohamed, M. A. & Mohamed, Y. M. A couple stress of peristaltic motion of Sutterby micropolar nanofluid inside a symmetric channel with a strong magnetic field and Hall currents effect. *Arch. Appl. Mech.* **91**, 3987–4010 (2021).
109. Parveen, N., Awais, M., Mumraz, S., Ali, A. & Malik, M. Y. An estimation of pressure rise and heat transfer rate for hybrid nanofluid with endoscopic effects and induced magnetic field: Computational intelligence application. *Eur. Phys. J. Plus* **135**(11), 1–41 (2020).
110. Arif, U., Nawaz, M., Alharbi, S. O. & Saleem, S. Investigation on the impact of thermal performance of fluid due to hybrid nanostructures. *J. Therm. Anal. Calorim.* **144**(3), 729–737 (2021).
111. Jayadevamurthy, P. G. R., Rangaswamy, N. K., Prasannakumara, B. C. & Nisar, K. S. Emphasis on unsteady dynamics of bioconvective hybrid nanofluid flow over an upward–downward moving rotating disk. *Numer. Meth. Partial Differ. Equ.* https://doi.org/10.1002/num.22680 (2020).
112. Nawaz, M. Role of hybrid nanoparticles in thermal performance of Sutterby fluid, the ethylene glycol. *Phys. A.* **537**, 122447 (2020).
113. Waqas, H., Farooq, U., Alghamdi, M. & Muhammad, T. Significance of melting process in magnetized transport of hybrid nanofluids: A three-dimensional model. *Alex. Eng. J.* **61**, 3949–3957 (2022).
114. Maxwell, J. C. On stresses in rarefied gases arising from inequalities of temperature. *Proc. R. Soc. Lond.* **27**, 304–308 (1878).
115. Smoluchowski, M. V. Ueber Wärmeleitung in verdünnten Gasen. *Ann. Phys.* **300**(1), 101–130 (1898).
116. Tekin, M. T., Botmart, T., Yousef, E. S. & Yahia, I. S. A comprehensive mathematical structuring of magnetically effected Sutterby fluid flow immersed in dually stratified medium under boundary layer approximations over a linearly stretched surface. *Alex. Eng. J.* **61**, 11889–11898 (2022).

117. Sajid, T. *et al.* Impact of gold nanoparticles along with Maxwell velocity and Smoluchowski temperature slip boundary conditions on fluid flow: Sutterby model. *Chin. J. Phys.* **77**, 1387–1404 (2022).
118. Brewster, M. Q. *Thermal Radiative Transfer and Features* (Wiley, 1992).
119. Elgazery, N. S. Flow of non-Newtonian magneto fluid with gold and alumina nanoparticles through a non-Darcian porous medium. *J. Egypt. Math. Soc.* **27**, 39 (2019).
120. Jamshed, W. *et al.* Entropy amplified solitary phase relative probe on engine oil based hybrid nanofluid. *Chin. J. Phys.* https://doi.org/10.1016/j.cjph.2021.11.009 (2021).
121. Jamshed, W. *et al.* A numerical frame work of magnetically driven Powell-Eyring nanofluid using single phase model. *Sci. Rep.* **11**, 16500 (2021).
122. Bilal, S., Sohail, M., Naz, R., Malik, M. Y. & Alghamdi, M. Upshot of Ohmically dissipated Darcy-Forchheimer slip ow of magnetohydrodynamic Sutterby fluid over radiating linearly stretched surface in view of Cash and Carp method. *Appl. Math. Mech.-Engl.* **40**, 861–876 (2019).
123. Keller, H. B. A new difference scheme for parabolic problems. In *Numerical solutions of partial differential equations* Vol. 2 (ed. Hubbard, B.) 327–350 (Academic Press, 1971).
124. Zaimi, K., Ishak, A. & Pop, I. Stretching surface in rotating viscoelastic fluid. *Appl. Math. Mech.* **34**, 945–[illegible] (20[illegible]).
125. Khan, N. S., Kumam, P. & Thounthong, P. Second law analysis with effects of Arrhenius activation energy and binary chemical reaction on nanofluid flow. *Sci. Rep.* **10**, 1226 (2020).
126. Ahmadi, A. A., Arabbeiki, M., Ali, H. M., Goodarzi, M. & Safaei, M. R. Configuration and optimization of a minichannel using water–alumina nanofluid by non-dominated sorting genetic algorithm and response surface method. *Nanomaterials* **10**, 901 (2020).
127. Bahiraei, M., Heshmatian, S., Goodarzi, M. & Moayedi, H. CFD analysis of employing a novel ecofriendly nanofluid in a miniature pin fin heat sink for cooling of electronic components: Effect of different configurations. *Adv. Powder Technol.* **30**, 2503–2516 (2019).
128. Dadsetani, R., Sheikhzadeh, G. A., Safaei, M. R., Leon, A. S. & Goodarzi, M. Cooling enhancement and stress reduction optimization of disk-shaped electronic components using nanofluids. *Symmetry* **12**, 931 (2020).
129. Goodarzi, M. *et al.* Boiling heat transfer characteristics of graphene oxide nanoplatelets nano-suspensions of water-perfluorohexane (C6F14) and water-n-pentane. *Alex. Eng. J.* **59**, 4511–4521 (2020).
130. Goodarzi, M. *et al.* Boiling flow of graphene nanoplatelets nano-suspension on a small copper disk. *Powder Technol.* **377**, 10–19 (2021).
131. Khan, H. *et al.* Effect of nano-graphene oxide and n-butanol fuel additives blended with diesel—Nigella sativa biodiesel fuel emulsion on diesel engine characteristics. *Symmetry* **12**, 961 (2020).
132. Li, Z. *et al.* Heat transfer evaluation of a micro heat exchanger cooling with spherical carbon-acetone nanofluid. *Int. J. Heat Mass Trans* **149**, 119124 (2020).
133. Li, Z. *et al.* Transient pool boiling and particulate deposition of copper oxide nano-suspensions. *Int. J. Heat Mass Trans* **155**, 119743 (2020).
134. Jathar, L. D. *et al.* Effect of various factors and diverse approaches to enhance the performance of solar stills: A comprehensive review. *J. Therm. Anal. Calorim* **147**, 4491–[illegible] (2022).
135. Alazwari, M. A., Abu-Hamdeh, N. H. & Goodarzi, M. Entropy optimization of first-grade viscoelastic nanofluid flow over a stretching sheet by using classical Keller-Box scheme. *Mathematics* **9**, 2563 (2021).
136. Farahani, S. D., Alibeigi, M., Zakinia, A. & Goodarzi, M. The effect of microchannel-porous media and nanofluid on temperature and performance of CPV system. *J. Therm. Anal. Calorim* **147**, 7945–7960 (2022).
137. Giwa, S., Sharifpur, M., Goodarzi, M., Alsulami, H. & Meyer, J. Influence of base fluid, temperature, and concentration on the thermophysical properties of hybrid nanofluids of alumina–ferrofluid: Experimental data, modeling through enhanced ANN, ANFIS, and curve fitting. *J. Therm. Anal. Calorim* **143**, 4149–4167 (2021).
138. Dadsetani, R. *et al.* Thermal and mechanical design of tangential hybrid microchannel and high-conductivity inserts for cooling of disk-shaped electronic components. *J. Therm. Anal. Calorim* **143**, 2125–2133 (2021).
139. Abu-Hamdeh, N. H. *et al.* A significant solar energy note on Powell-Eyring nanofluid with thermal jump conditions: Implementing Cattaneo-Christov heat flux model. *Mathematics* **9**, 2669 (2021).

Author contributions

W.J. formulated the problem. W.J. and M.R.E. solved the problem. W.J., M.R.E., R.S., A.A.P., M.A., Z.R., S.S.P.M.I., and W.W. computed and scrutinized the results. All the authors equally contributed in writing and proof reading of the paper. All authors reviewed the manuscript.

Competing interests

The authors declare no competing interests.

Additional information

Correspondence and requests for materials should be addressed to W.W.

Reprints and permissions information is available at www.nature.com/reprints.

Publisher's note Springer Nature remains neutral with regard to jurisdictional claims in published maps and institutional affiliations.